



Room temperature stability, structure and mechanical properties of cubic tungsten carbide in flash sintered products

Isacco Mazo^{1,*} Jon M. Molina-Aldareguia^{2,3}, Alberto Molinari¹, and Vincenzo M. Sglavo^{1,4}

¹ Department of Industrial Engineering, University of Trento, Via Sommarive 9, 38123 Trento, Italy

² IMDEA Materials Institute, C. Eric Kandel 2, 28906 Getafe, Madrid, Spain

³ Department of Mechanical Engineering, Universidad Politécnica de Madrid, C. de José Gutiérrez Abascal, 2, 28006 Madrid, Spain

⁴ INSTM, Via G. Giusti 9, 50121 Florence, Italy

Received: 2 November 2022

Accepted: 19 December 2022

Published online:

4 January 2023

© The Author(s), under exclusive licence to Springer Science+Business Media, LLC, part of Springer Nature 2023

ABSTRACT

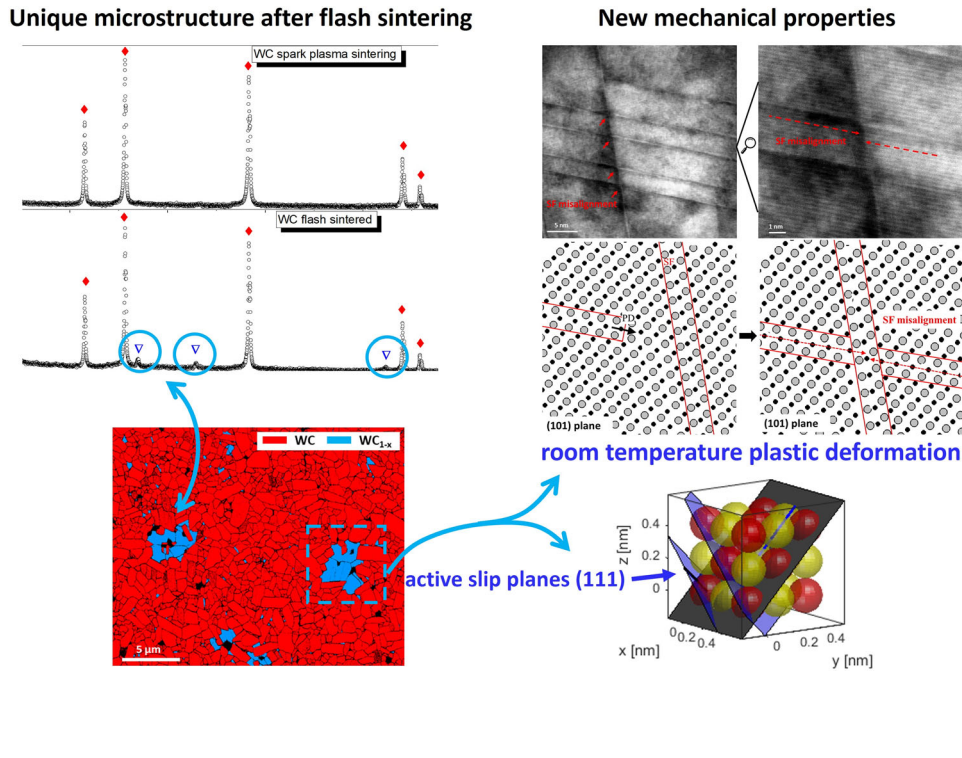
This work explores the possibility to obtain the metastable cubic tungsten carbide phase (WC_{1-x}) during the rapid and the ultrarapid consolidation of hexagonal WC nanopowders. Spark plasma sintering and flash sintering techniques are implemented to study the formation and the stability of WC_{1-x} during sintering. A biphasic ceramic material, corresponding to cubic-WC/hex-WC (10/90 vol%), can be obtained uniquely with the flash sintering process. The ultrafast sintering of powders containing Cr and V impurities results in a peculiar cubic WC quaternary phase ($W_{0.87}Cr_{0.12}V_{0.09}C_{0.71}$) which retains the crystalline structure, $Fm\bar{3}m\{225\}$, and the metastable character of WC_{1-x} , decomposing into the thermodynamically stable hexagonal phases (WC and W_2C) after vacuum annealing at 700 °C and 1100 °C. Structural features of the composite are analysed by HRTEM and Transmission Kikuchi Diffraction (TKD), which pointed out the activation of room-temperature plastic deformation mechanisms in cubic WC grains. Such behaviour is connected to stacking faults interacting with partial dislocations on {111} planes, similarly to FCC metals. Nanomechanical indentations were also used to map the elastic modulus and the hardness of the cubic phase, which shows a noticeable softer character with respect to the hexagonal matrix. These results suggest flash sintering as a new strategy for producing WC/ WC_{1-x} composite materials with tailored elastic modulus and hardness/toughness ratio.

Handling Editor: Megumi Kawasaki.

Address correspondence to E-mail: isacco.mazo@unitn.it

E-mail Addresses: jon.molina@imdea.org; alberto.molinari@unitn.it; vincenzo.sglavo@unitn.it

GRAPHICAL ABSTRACT



Introduction

The high-temperature cubic tungsten carbide phase, WC_{1-x} , is thermodynamically stable only between 2789 and 3028 K and in sub-stoichiometric carbon concentration condition (37–50 at%) [1]. This phase was found to remain stable at room temperature only in peculiar conditions of very fast cooling rate or quenching from the molten state; Zhang et al. suggested that a cooling rate as high as 10^8 – 10^{11} K/s is necessary to stabilize the cubic lattice [2]. Cubic WC_{1-x} nanopowders were successfully synthesized by Pak et al. by discharge plasma jet [3]. Tanaka et al. exploited the high temperature and speed generated by the electrical explosion of a W wire immersed in a paraffin bath [4]. Evidence of this metastable phase was also found after high energy laser/ion beam surface treatments of WC components [2, 5]. Lian et al. proposed a novel approach to produce ultrafine WC_{1-x} particles (3–4 nm) by simply pyrolysis of dicyandiamide mixed with ammonium

metatungstate at 800 °C [6]. Besides the important achievements reported in the production and study of this metastable phase, the knowledge about its physical and mechanical properties is rather scarce if not absent at the moment. Its further study is limited by the absence of a proper route to produce the cubic polymorph in bulk components. Although different routes are present for the production of WC_{1-x} in form of nanopowders, their sintering inevitably leads to the transformation of the WC_{1-x} into WC and W_2C products. The thermal stability of WC_{1-x} layers obtained by magnetron sputtering was studied by Abad et al. who pointed out its phase transition around 700 °C, well below a suitable temperature for sintering [7].

Flash sintering (FS) offers a new opportunity for the retention of metastable phases at room temperature, ultrafast heating rates and non-equilibrium generation of lattice defects allowing the consolidation of out-of-equilibrium materials [8, 9]. Flash sintering conditions have been very recently achieved in tungsten carbide during electrical resistance sintering

(ERS) experiments, thus opening the possibility to study the conditions of existence of cubic WC_{1-x} in the sintered products [10]. The use of WC powders containing small amount of oxides (5 wt%) allowed the generation of biphasic WC/W₂C (60/40 vol%) sintered bodies. Oxide species were shown to be responsible for a carbon loss at high temperature, associated with prominent decarburization of the stoichiometric WC lattice. The carbon stability range of the cubic phase sits in between the two hexagonal phases, WC and W₂C [1]. Therefore, the FS process was used in the current work to sinter commercial WC powders with lower oxygen content trying to avoid the generation of W₂C in favour of the WC_{1-x} phase. This work aims at pointing out how flash sintering can induce the formation of the metastable high-temperature phase, WC_{1-x} , for opportune carbon concentration. Structural features are analysed by HRTEM and Transmission Kikuchi Diffraction (TKD) and nanoindentations are used to determine elastic modulus and the hardness of the cubic phase to be compared with the mechanical properties of the hexagonal one.

Materials and methods

Tungsten carbide nanopowders were purchased from Inframaterial Advanced Materials®, product number #74 N-0601 [11]. The chemical composition of the starting powder was characterized by EDXS (ThermoFischer® Apreo 2S LoVac) at 20 kV and 3.2nA. The phase composition of powders and sintered products was determined by X-ray diffraction (PANalytical EMPYREAN), with Cu-K α 1 (1.54060 Å) radiation generated at 45 kV and 40 mA in a line focus configuration. The samples were analysed in a Bragg–Brentano geometry, by using an angular step size of 0.012° and an accumulation time of 100 s. The 1-D diffraction patterns were refined by the Rietveld method (HighScore Plus® software) using the following ICDD diffraction cards as reference patterns: 01-084-5996 for WC, 00-035-0776 for α -W₂C and 00-020-1316 for cubic WC_{1-x} .

The electrical resistance flash sintering (ERFS) process was performed in a specifically realized apparatus where the sample (uniaxially pressed pellet) is densified by the application of an alternated current. The sintering process takes place within a zirconia die, the pellet being subjected to the pressure

exerted though two cylindrical electrodes to maintain the electrical contact. In the present work, cylindrical pellets produced by uniaxial pressing 1.3 g of powder were inserted into the zirconia die and flash sintered for 10 s under 4 MPa uniaxial pressure by controlling the maximum voltage and current to 3.7 V and 1000 A, respectively. A more detailed description of the ERFS apparatus and methodology is reported in previous works [10, 12, 13].

The same powder was also consolidated by Spark Plasma Sintering (SPS) at K4Sint SpA (Pergine Valsugana, Italy) by means of a Dr. Sinter 1050 apparatus. The sintering was carried out in low vacuum condition (5×10^{-4} bar), under 60 MPa uniaxial pressure according to the following heating/cooling cycle: (i) rapid heating (200 °C /min) from room temperature to 2100 °C, (ii) 5 min of holding time at 2100 °C and (iii) cooling from 2100 °C to room temperature in 15 min.

Sintered products were cut in the direction of the applied pressure, and the obtained cross sections were grinded and polished with diamond abrasive pastes down to 1 μm size. Polished surfaces were analysed by means of FEG-SEM microscope (ThermoFischer® Apreo 2S LoVac) equipped with an EBSD detector for the analysis of the phases and grains orientation.

The thermal stability of the flash sintered samples was evaluated by vacuum annealing experiments in a tubular furnace (Nabertherm RHTH 120–600/16) at the temperatures of 400, 700 and 1100 °C with 1 h of holding time.

Mechanical properties in specific areas were evaluated by nanoindentation (Hysitron triboindenter TI950), mapping the elastic modulus and the hardness with a Berkovich diamond tip (BKL-DLC). Preliminary cyclic loading–unloading procedures were performed for the correction of the machine compliance and for the estimation of suitable penetration depth to avoid indentations overlapping. Maps were acquired in an area of $7.7 \times 7.7 \mu\text{m}^2$, by using 3 mN maximum load; 22 × 22 indents were produced with a separation distance of 0.35 μm. The indentation map position was calibrated by imaging the surface with the same indenter diamond tip in AFM mode.

The deformation behaviour of the grains at the nanoscale was assessed by preparing an electron transparent lamella of a plastically deformed portion of material. To pursue this scope, firstly, a micropillar

was prepared by focused ion beam (FIB) milling within a FIB-SEM dual column microscope (Helios NanoLab 600i). Pillars of 3 μm in diameter and 6 μm in height were then compressed uniaxially by a diamond punch (\varnothing 15 μm) within the apparatus for nanoindentation (Hysitron triboindenter TI950), with a strain rate of 10^{-4} s^{-1} . The compression tests were stopped after reaching the yield point ($\varepsilon = 0.2\%$) and before the final brittle failure. A lamella was prepared on the cross section of the deformed pillar by FIB milling: the current and the accelerating voltage were scaled down from 30 kV and 9.3 nA to 10 kV and 80 pA to reach electron transparency and to limit the ion damage of the material.

High-resolution TEM/STEM micrographs and EDXS analysis were obtained from the prepared lamella at 200 kV in a FEI Talos F200x microscope. The orientation and crystalline composition of the grains composing the lamella were finally characterized by the Transmission Kikuchi Diffraction

technique, also known as transmission EBSD, in the FEG-SEM microscope. Transmission Kikuchi patterns were obtained following the indication of Suzuki [14]: the lamella was positioned at a WD of 5 mm between the electron beam and the EBSD detector, with a tilting angle of 25° with respect to the horizontal axis. The pattern was acquired with an accelerating voltage of 30 kV and a step size of 0.025 μm .

Results and discussion

Powder composition

The tungsten carbide nanopowders used in the present work show a very limited oxygen content ($0.34 \pm 0.01 \text{ wt\%}$), much lower if compared to those previously tested in flash sintering experiments (2–3 wt%) [10]. EDXS analysis (Fig. 1) also shows the presence of Cr and V impurities, in very low

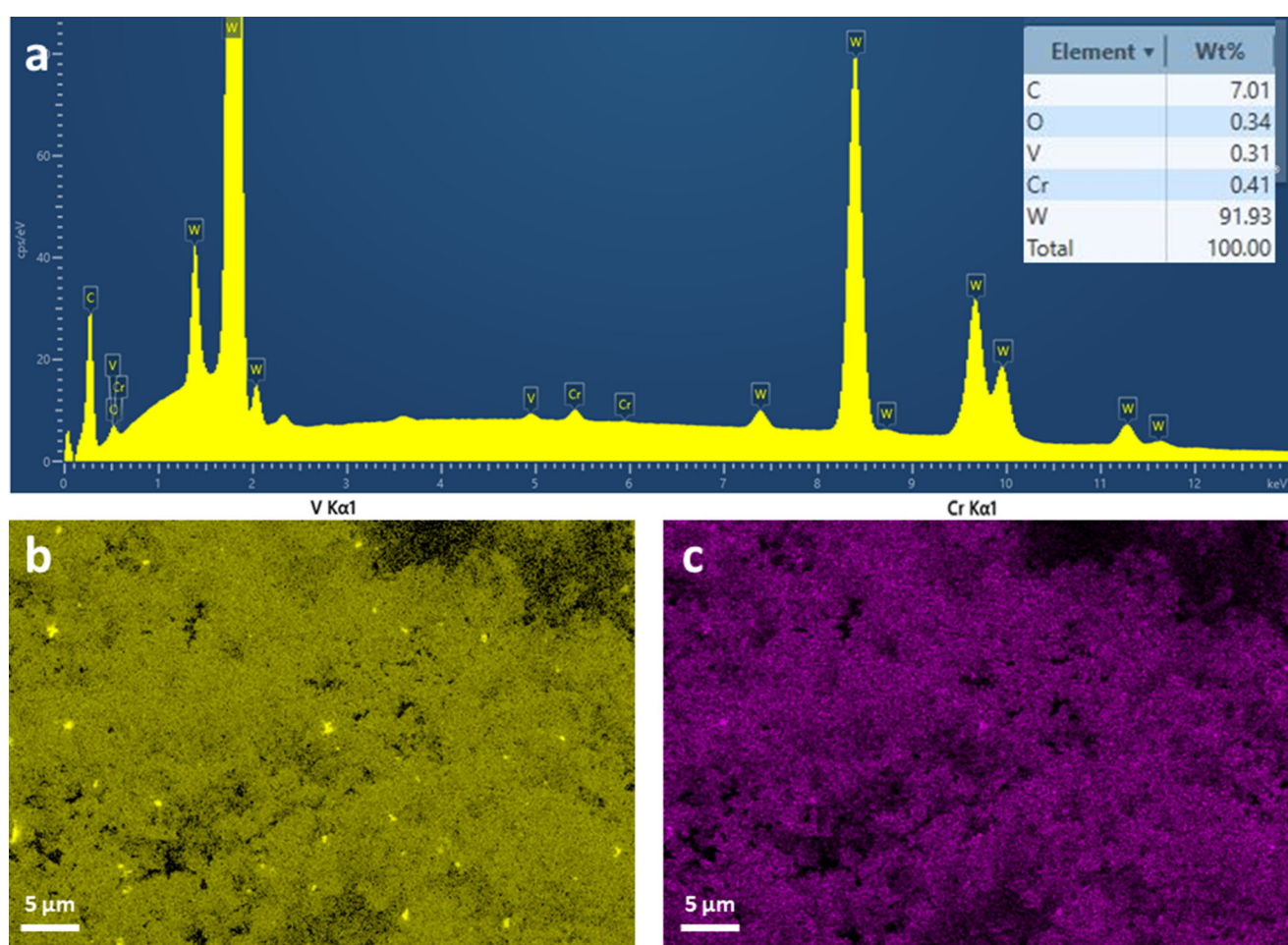


Figure 1 EDXS elemental spectrum of WC powder (a), elemental map of V (b) and of Cr (c).

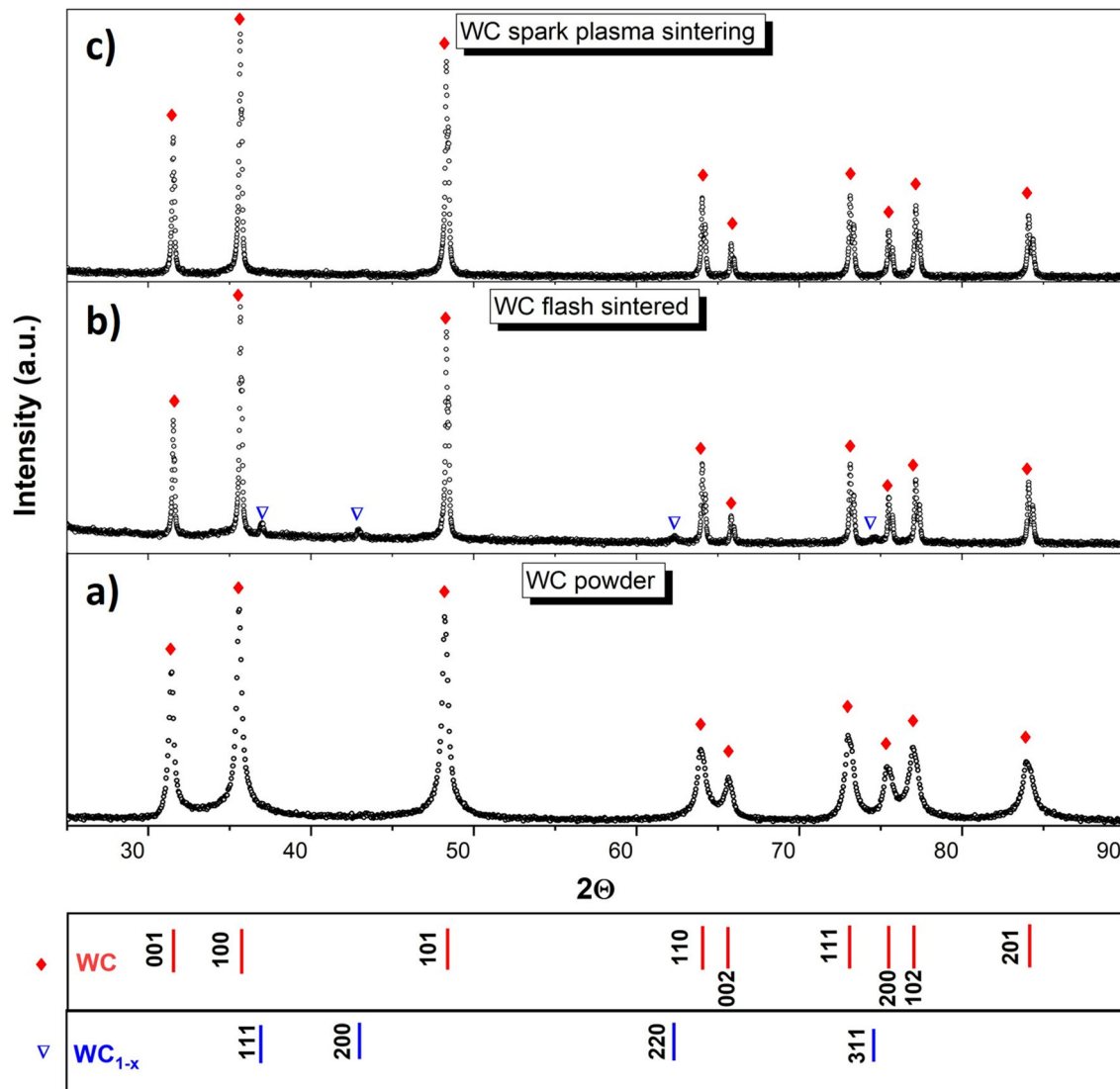


Figure 2 XRD spectra of WC powder (a) and bulk components obtained by flash sintering (b) and spark plasma sintering (c).

quantities (0.4 and 0.3 wt%, respectively). These are not homogeneously dispersed in the powder and are present also as small spots. The XRD analysis (Fig. 2a) shows the absence of any Cr and V oxide or carbide, thus suggesting the presence of these impurities as single elements dispersed in the WC matrix. Despite these contaminants, the powder is characterized by a very high purity level, 98–99 wt% (Fig. 1a), and composed exclusively of WC hexagonal phase (Fig. 2a).

The phase composition of the samples processed by electrical resistance flash sintering (ERFS) and spark plasma sintering (SPS) is shown in Fig. 2b,c. The low initial oxygen content and the absence of any tungsten oxides in the starting powder avoid the

decarburization of WC in the low carbide phase W_2C during the SPS process. This result demonstrates how, by using high purity WC powder, fully monophasic (100% h-WC) sintered products are obtained by SPS. Other researchers reported the necessity to control the decarburization by precisely tuning carbon addition to the initial powders [15].

Presence and structure of cubic WC_{1-x} phase after flash sintering

The ultrarapid consolidation by the ERFS process results in the formation of a new phase. Peaks of low intensities appear at 37.0° , 42.9° , 62.4° and 74.6° (Fig. 2b) together with typical hexagonal WC reflexes.

Said peaks cannot be fitted by any W₂C polymorph, but they correspond to the metastable high-temperature WC_{1-x} cubic phase-space group Fm-3 m {225}, being indexed by using ICDD card no. 00-020-1316 (cross-referenced to 04-022-5716), the same card used to characterize cubic WC_{1-x} nanoparticles obtained by discharge plasma jet synthesis [3]. The cubic phase, differently from the hexagonal one, has a broad range stability. This is narrow at the lowest transformation temperature (2789 K), corresponding to WC_{0.58}–WC_{0.65}, and wider WC_{0.59}–WC_{0.98–1.00} from 3030 to 3055 K [1]. The lattice parameter of the cubic modification ($a_{WC_{1-x}}$) was studied accurately by Kurlov and Gusev [1] for several carbon concentrations, and the data are well fitted by the following function:

$$a_{WC_{1-x}} = 0.4015 + 0.0481y - 0.0236y^2 [\text{nm}] \quad (1)$$

where $y = 1 - x = C/W$ refers to the C atomic concentration in the cubic lattice. Equation 1 can be used to estimate the carbon stoichiometry using the lattice parameter evaluated from XRD measurement. The reference lattice parameter of the phase used for the fitting (no. 04-022-5716) is $a_{\text{ref}} = 4.234 \text{ \AA}$, while the Rietveld refining of pattern in Fig. 2 (b) gives $a_{\text{exp}} = 4.211 \text{ \AA}$ (Fig. 4). This lattice constant is lower than every other value reported so far: Pak et al. [3] obtained $a = 4.2536 \text{ \AA}$ for cubic WC_{0.86}, Rudy et al. determined a value of $a = 4.220 \text{ \AA}$ for WC_{0.61} and, according to Sara et al., the lower phase boundary is WC_{0.59}. However, the use of Eq. 1 with the parameter measured for the flash sintered WC_{1-x} of Fig. 2b results in WC_{0.56}, where the carbon content (C = 36 at%) is outside the WC_{1-x} phase stability region, between β -W₂C and γ -WC_{1-x} (Fig. 5) [1]. The discrepancy of the lattice constant from the data regarding the high temperature phase stability in the W–C system can be explained by the results shown in Figs. 3, 4.

EBSD analysis successfully detects the presence of cubic phase within the WC matrix by using again the pattern no. 04-022-5716 as a reference. Well-developed WC_{1-x} grains are present among the hexagonal WC grains. The micrograph shown in Fig. 3 is representative of the entire cross section, where WC_{1-x} grains are mainly organized in small clusters of 5–12 grains and rarely isolated within the WC matrix.

The EDS maps acquired on the same area reveal a certain amount of Cr and V, the same elements identified initially in the powder. Nevertheless, the comparison of elemental maps in Fig. 1b, c with that

of Fig. 3 points out the difference in the dispersion of such elements, segregated in specific grains, that, according to EBSD analysis, belong to the cubic phase. This segregation can be for sure ascribed to a very fast atomic diffusion of such two elements in the cubic phase during the flash sintering process. Considering that the entire ERFS process duration is only 10 s and that Cr and V are initially dispersed randomly in the powder (Fig. 1), their segregation must have occurred with an unconventionally high diffusional rate. The concentration of these elements in some specific grains can modify the crystalline structure of the detected phase. For this reason, the diffraction pattern of Fig. 2b was tentatively refined with other cubic phases, symmetry Fm-3 m {225}, containing Cr and V, like chromium tungsten carbide (Cr_{0.4}W_{0.6}C) and vanadium tungsten carbide (V_{0.5}W_{0.5}C). The diffraction lines of these two phases are shown in Fig. 4. The most intense peaks can be precisely fitted by the initial pattern of the reference card no. 04-022-5716, although it is possible to observe how the exact peak positions of the detected phase slightly diverge from the WC_{1-x} pattern with a position between cubic V_{0.5}W_{0.5}C and Cr_{0.4}W_{0.6}C phases (Table 1).

The substitution of W with Cr or V in the cubic lattice shifts the peaks to higher 2θ values, Cr having the strongest effect on their position and cell parameter (Table 1). The central position of the experimentally determined phase with respect the V_{0.5}W_{0.5}C and Cr_{0.4}W_{0.6}C phases suggests the presence of a new cubic phase in the flash sintered product, belonging to the quaternary system comprising W–C–Cr–V, where Cr and V partially substitute W, modifying the original structure of WC_{1-x}. To support such hypothesis, a new phase was created with the HighScore® software, starting from a space group Fm-3 m {225} and a lattice parameter $a = 4.2110 \text{ \AA}$. Cr and V atoms were assumed to be present in the cubic lattice in substitution of W ones. The degree of substitution was assessed by refining (Rietveld method) the occupancy of Cr and V in the W sites. The simulated pattern confirmed the presence of a new phase, where the substitutional degree of Cr and V can be estimated between (W_{0.8}Cr_{0.1}V_{0.1})C and (W_{0.6}Cr_{0.2}V_{0.2})C. Figure 4 shows that the new quaternary phase, referred to as (W_{0.8}Cr_{0.1}V_{0.1})C for simplicity, matches almost perfectly the 111, 200, 220 and 311 diffraction peaks (Table 1). The segregation of Cr and V during flash sintering affects the WC

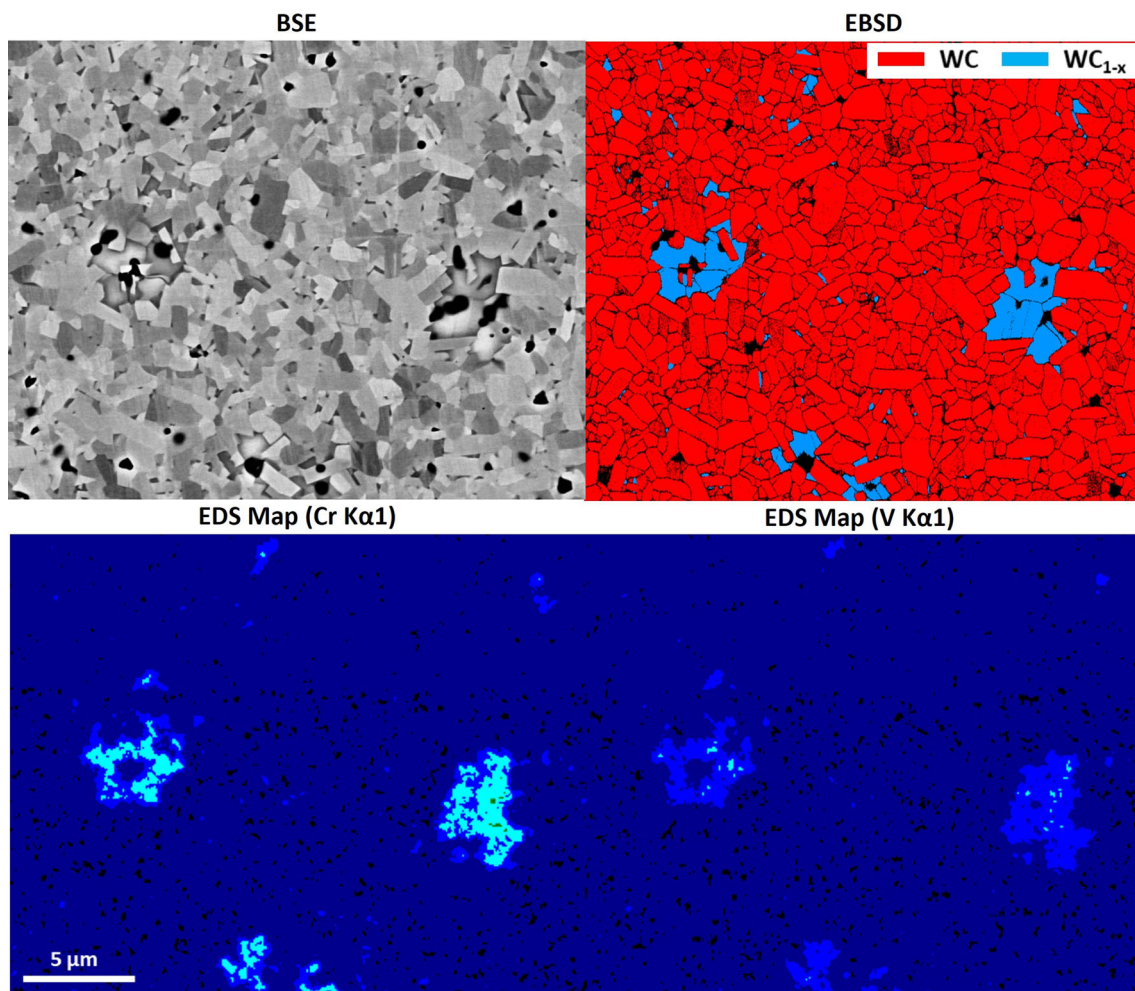


Figure 3 Microstructure analysis of the polished cross section prepared by the ERFS process. Back-scattered electrons (BSE) image is compared with EBSD and EDS maps to point out the

presence and the composition of the cubic phase (WC_{1-x}) in the flash sintered product.

Figure 4 Magnified view of the XRD peaks of Fig. 2b for the cubic WC phase. Comparison between the diffraction line positions of the reference patterns shown in the legend and the experimental one.

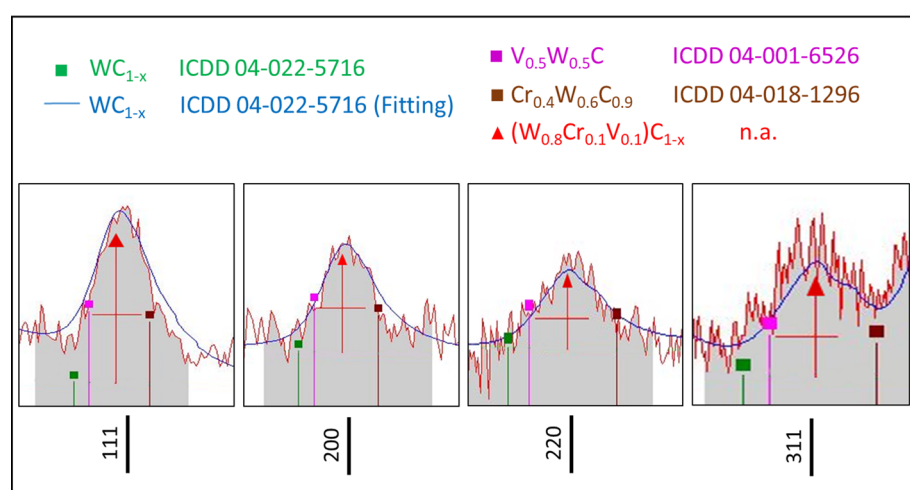


Table 1 Lattice constant and diffraction lines position of the reference patterns and the experimental XRD data

Phase	a [Å]	Density [g/cm ³]	111 [2θ]	200 [2θ]	220 [2θ]	311 [2θ]
WC _{1-x}	4.234	17.139	36.735	42.674	61.937	74.225
V _{0.5} W _{0.5} C	4.226	11.388	36.807	42.759	62.067	74.389
Cr _{0.4} W _{0.6} C _{0.9}	4.1935	12.787	37.107	43.112	62.611	75.075
(W _{0.8} Cr _{0.1} V _{0.1})C _{1-x}	4.2119	15.055	36.939	42.914	62.304	74.683
Experimental pattern	4.2110	n.a	36.932	42.9064	62.291	74.670

cubic structure, shifting the peak position and decreasing the calculated density of WC_{1-x} from 17.12 g/cm³ to 15.05 g/cm³ (Table 1).

The discrepancy in the result obtained from Eq. 1 will be discussed in “TEM & Transmission Kikuchi Diffraction (TKD) analyses” section together with the precise evaluation of Cr, V and C content. It will be shown how the modification in the cell parameter introduced by Cr and V can be included into Eq. 1, to correctly estimate the carbon content of the cubic phase.

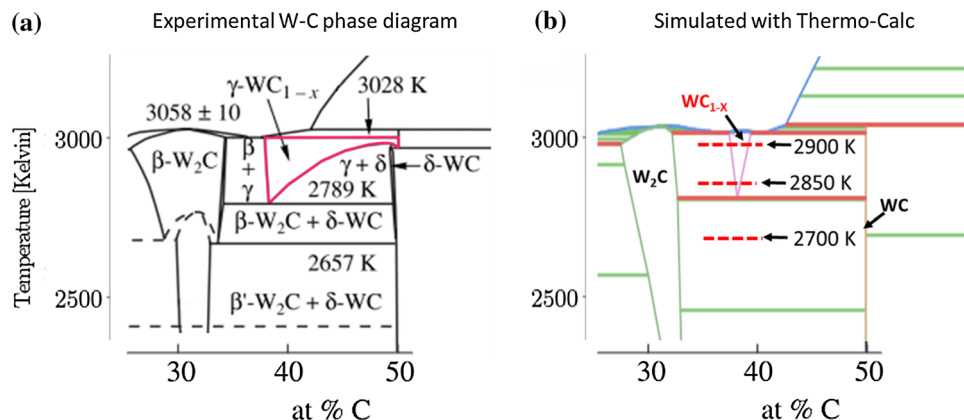
Formation of WC_{1-x} and its stability

Differently from the sample consolidated under flash sintering conditions, those prepared by SPS (Fig. 2c) do not show any presence of this new WC_{1-x} cubic phase. Its absence implies that the phase transformation WC → WC_{1-x} cannot occur at the SPS sintering temperature or that the cubic phase decomposes upon cooling. Of the two hypotheses, the former is more likely since (i) the maximum temperature reached during SPS is 2100 °C, while WC_{1-x} is thermodynamically stable only above 2515 °C (Fig. 5) and (ii) WC_{1-x} decomposes in multiple products, WC, W₂C and W, which are not detected in the sintered material (Fig. 2c). Data regarding the thermal stability of WC_{1-x} are currently limited to thin films,

produced by low-temperature sputtering, or to nanoparticles. Abad et al. [7] reported a transformation of WC_{1-x} thin films in W₂C and WC products during vacuum annealing at 700 °C and a second reaction at 900–1000 °C with the formation of metallic tungsten. Shanenkov et al. [16] showed how the thermal stability under vacuum of WC_{1-x}, in the form of nanoparticles can be extended up to 1500 °C in the presence of carbon shell. However, in the same study they revealed how, in the attempt to sinter WC_{1-x} nanoparticles, full decomposition into W₂C and WC products occurred after SPS at 1500 °C. The diffusional phenomena during sintering promote the decomposition of WC_{1-x} at lower temperatures. Attempts to consolidate almost pure (94 + %) WC_{1-x} nanoparticles at 1500 °C by SPS resulted in low density (74%) sintered bodies composed exclusively of WC and W₂C [16]; this leads to the conclusion that SPS is not a viable route for the formation or the retention of cubic tungsten carbide.

Conversely, flash sintering appears capable of producing cubic tungsten carbide phase very similar to WC_{1-x}, namely (W_{0.8}Cr_{0.1}V_{0.1})C, simply starting from hexagonal WC nanopowders. In addition, very interestingly, this new phase remains stable, or probably better, metastable, upon cooling down to room temperature. However, its existence in the sintered products requires to discuss the

Figure 5 W–C phase diagram corrected with experimental data as reported by Kurlov and Gusev [1] (a) and W–C phase diagram simulated with Thermo-Calc (b).



simultaneous presence of Cr and V on the phase stability. Chromium tungsten carbide and vanadium tungsten carbide are known phases in the W-Cr-C and W-V-C systems although, according to the international centre for diffraction data (ICDD), updated to 2021, a quaternary phase comprising W-Cr-V-C has not been reported yet. For this reason, the effect of Cr and V on the thermodynamic stability of the cubic WC_{1-x} was simulated with the CAL-PHAD method using the Thermo-Calc software (TCNI8 database). The experimentally determined W-C phase diagram [1] and its simulated counterpart are shown in Fig. 5. The W-C phase diagram and the temperature stability range for WC_{1-x} were simulated with a sufficient accuracy by using the cited database, although the simulation lacks of the accuracy of the experimental phase diagram in describing the stability range of WC_{1-x} between 40 and 50 at% C. Figure 6 shows how Cr and V affect the temperature stability range of WC_{1-x} at three different temperatures, 2700, 2850 and 2900 K. Specifically, a small concentration of Cr (1–2 at%) in solid solution suppresses completely the existence of WC_{1-x} in the

2850–2900 K temperature range; conversely, V has the opposite effect, it allowing the retention of the cubic phase also at temperatures lower than 2700 K, below the transformation temperature of the original phase diagram (Fig. 5b). However, the attempt to estimate the stability of the quaternary phase, $(W_{0.8}Cr_{0.1}V_{0.1})C$, did not give reliable results due to a lack of information in the available database.

The stability of this phase in the range from 25 up to 1100 °C was further determined by vacuum annealing experiments and subsequent XRD analyses of the flash sintered specimen. According to Fig. 7, the $(W_{0.8}Cr_{0.1}V_{0.1})C$ phase is stable up to about 700 °C and then decomposes to more stable phases. Between 700 °C and 1100°C $(W_{0.8}Cr_{0.1}V_{0.1})C$ completely disappears with the formation of W_2C phase. These results well agree with those of Abad et al. [7] who observed that WC_{1-x} decomposes in the same temperature range into WC and W_2C . $(W_{0.8}Cr_{0.1}V_{0.1})C$ is demonstrated to be a metastable phase and, similarly to pure cubic tungsten carbide (WC_{1-x}), it possesses a comparable temperature transformation range and the same decomposition products.

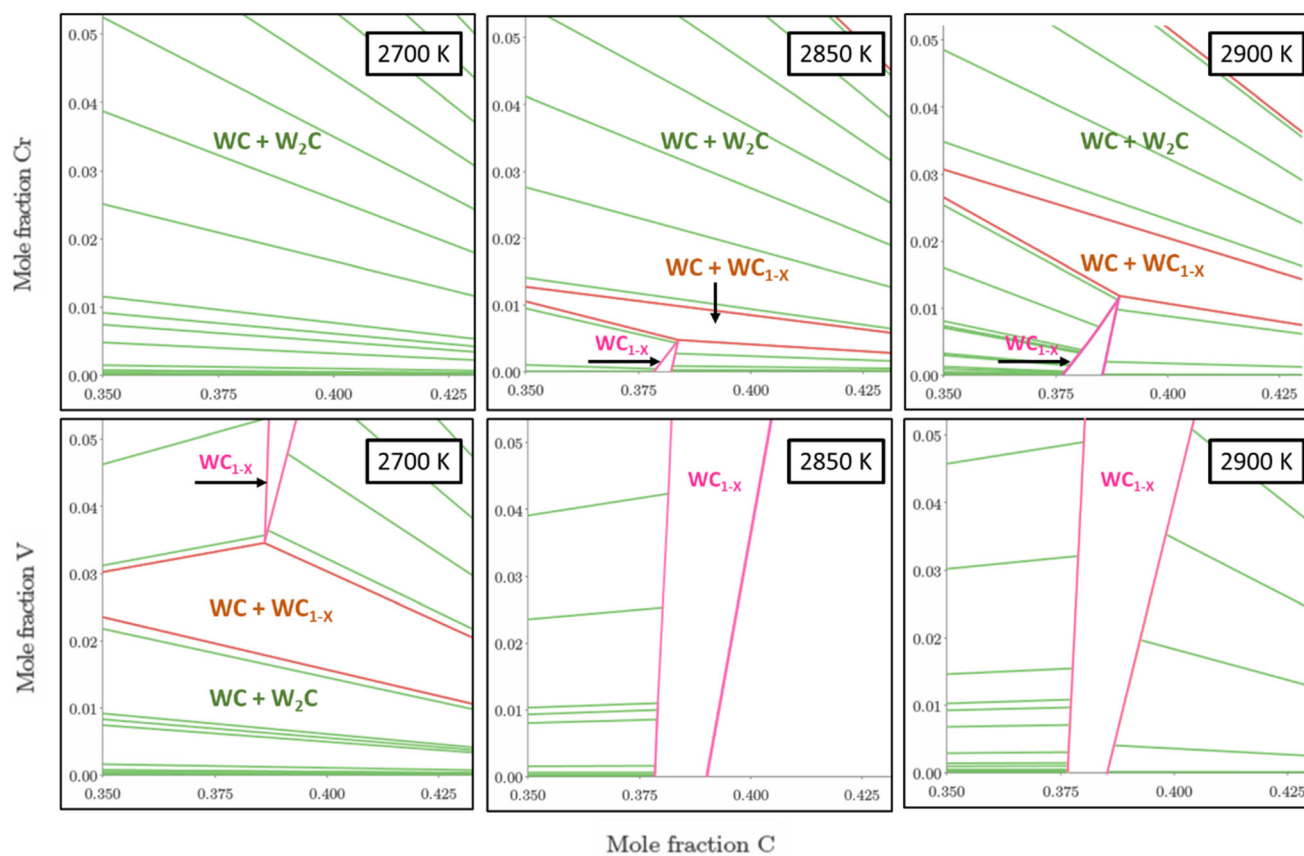


Figure 6 Ternary phase diagrams for W-Cr-C and W-V-C at 2700, 2850 and 2900 K.

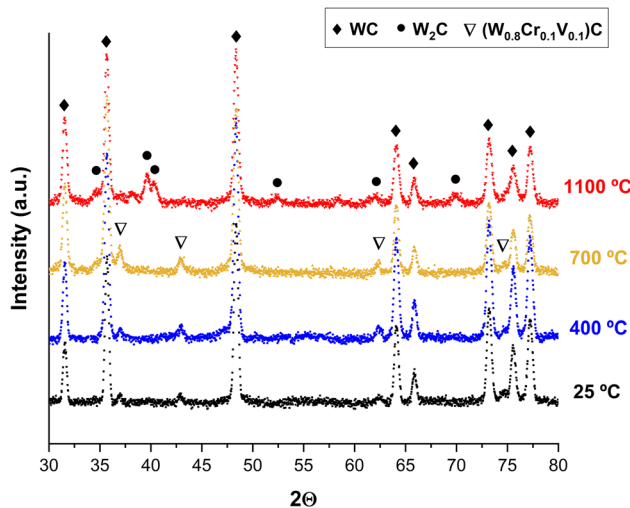


Figure 7 XRD analyses of as-produced flash sintered WC samples and after vacuum annealing at 400, 700 and 1100 °C.

Since VC and Cr_3C_2 are well-known grain growth inhibitors for WC-based products, several researchers studied the formation of secondary new phases in the W–C–Cr–V system. The simultaneous effect of Cr and V addition in WC products sintered by SPS was studied by Al-Aqeeli and he did not find any presence of other phases in addition to hexagonal WC [17]. Sugiyama et al. evidenced how only few atomic layers, at the WC–Co interface, are affected by V addition, resulting in a $(\text{W}, \text{V})\text{C}_x$ layer with a NaCl crystal structure [18]. The same evidence for a $(\text{Cr}, \text{W})\text{C}$ ultrathin layer (1.4 nm) formed on the WC grain surface in contact with the Co-rich binder phase was found by Yousfi et al. [19]. Several researcher proposed that the cubic $(\text{Cr}, \text{V}, \text{W})\text{C}$ layers, occurring at the WC–Co and WC–WC interface, act as grain inhibitors in cemented carbides [20]. Similarly, but in the absence of any additive, Gao et al. pointed out how at WC–Co and WC–WC interfaces the formation of a layer-like cubic WC_{1-x} , of few atomic planes, is energetically favoured and stabilized [21]. WC_{1-x} and its V and Cr alternatives retain stability due to low surface energy and coherent relationships between the involved interfaces. Based on this background and on the strong similarities regarding crystalline structure, metastability and decomposition products between $(\text{W}_{0.8}\text{Cr}_{0.1}\text{V}_{0.1})\text{C}$ and WC_{1-x} (Figs. 4, 6, 7), the influence of Cr and V on the room temperature stability of cubic tungsten carbide can be excluded. In this perspective, the flash sintering process has a double potential: (i) it allows the transformation $\text{WC} \rightarrow \text{WC}_{1-x}$ to occur during sintering and (ii) it

preserves the metastable phase during the cooling process.

Flash sintering has been proposed as a defects engineering technology capable of producing new material features and properties by the alteration of the lattice defects equilibrium. Noticeable is the modification of plastic deformation mechanisms driven by the introduction of a vast amount of defects [22–24], or the achievement of a non-equilibrium thermodynamic state in entropy-stabilized oxides [25]. In this context, Fig. 8 compares the crystal quality (microstrain) between WC sample and phases obtained during the flash sintering process and during SPS. The quantification of the lattice defects can be accomplished by analysing the line broadening dependency on the diffraction peaks angle in Fig. 2. The contribution of size and strain on the overall peak broadening (B_{struct}) can be separated by plotting $B_{\text{struct}} \cos \theta$ as a function of $\sin \theta$ according to the equation:

$$B_{\text{struct}} \cos \theta = 1.1 \frac{\lambda}{\text{crystallite size}} + \text{lattice strain } (4 \sin \theta) \quad (2)$$

in the so-called Williamson-Hall plot (Fig. 8).

For a correct interpretation of the peak broadening and to exclude the contribution of instrumental broadening, a zero microstrain reference sample was produced: well annealed WC, with average grain size of 20 μm , was obtained after 2 h sintering at 2150 °C in a pressure-less vacuum furnace (Astro®). Crystalline defects were quantified by the slope of the

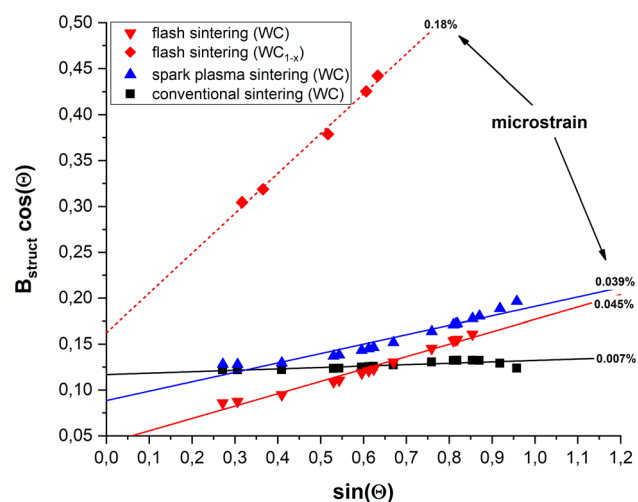


Figure 8 Linear Williamson-Hall plot: discrimination of the size and defects broadening contribution to XRD peaks.

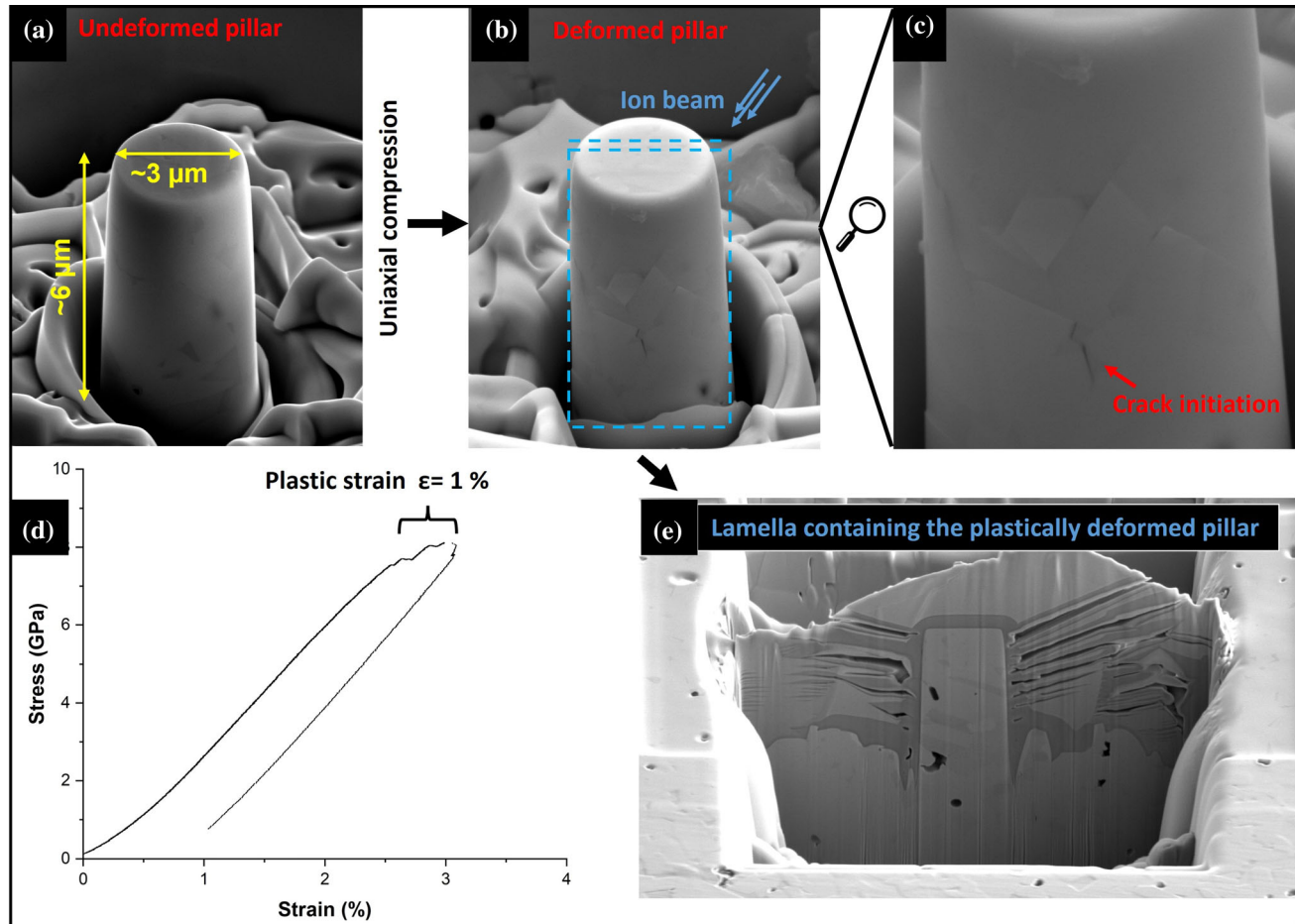


Figure 9 Procedure for studying the small-scale deformation behaviour of tungsten carbide grains. An electron transparent portion of the material, namely a “lamella” (e) was prepared by focused ion beam (FIB) on a pillar (a) which was preliminarily

lines in the Williamson-Hall plot (W-H) in Fig. 8. The conventionally sintered material is certainly a good standard for the microstrain analysis, being the corresponding line in the W-H plot almost flat. Regarding the hexagonal WC phase, samples sintered by ERFS are characterized by a slightly higher amount of lattice defects (microstrain) with respect to those obtained by SPS. Conversely, the line corresponding to the cubic phase strongly diverges from the hexagonal phase, showing a vast contribution of post sintering defects to its crystal quality. Hexagonal WC is known to be characterized by an anomalous low concentration of defects in both metal and carbon sublattices. The formation energy of V_C (carbon vacancies) is significantly lower than for V_W and, therefore, any possible deviation from the stoichiometry is mediated by C defects in the form of vacancies. Since in WC the carbon stability range as

uniaxially deformed (b) above the elastic limit (d). A magnified view of the deformed pillar (c) points out the initial stage of controlled crack propagation in the deformed pillar.

narrow as a line (Fig. 5), very small deviations from stoichiometry are allowed. An anomalous low defect concentration in hex-WC crystals was accurately determined by positron annihilation spectroscopy [26] and by density functional theory (DFT) calculations [27]. Indeed, the flash sintering process only allows the introduction of a limited amount of “extra-defects” in the sintered products compared to SPS. Conversely, the WC_{1-x} phase, which is characterized by its carbon vacancies and by the additional substitutional defects of Cr and V, as previously determined, can accommodate lattice defects much more easily. Correspondingly, the cubic phase results in a defect population one to two orders of magnitude larger than in the hexagonal counterparts.

The metastable character (Fig. 7) and the unconventional high density of lattice defects (Fig. 8) of the cubic phase ($W_{0.8}Cr_{0.1}V_{0.1})C_{1-x}$) stimulate the idea of a

Figure 10 STEM micrograph (a) and TDK analysis (b) of a lamella containing a significant portion of cubic grains. The red boxes (1 & 2) show the areas selected for the successive analyses.

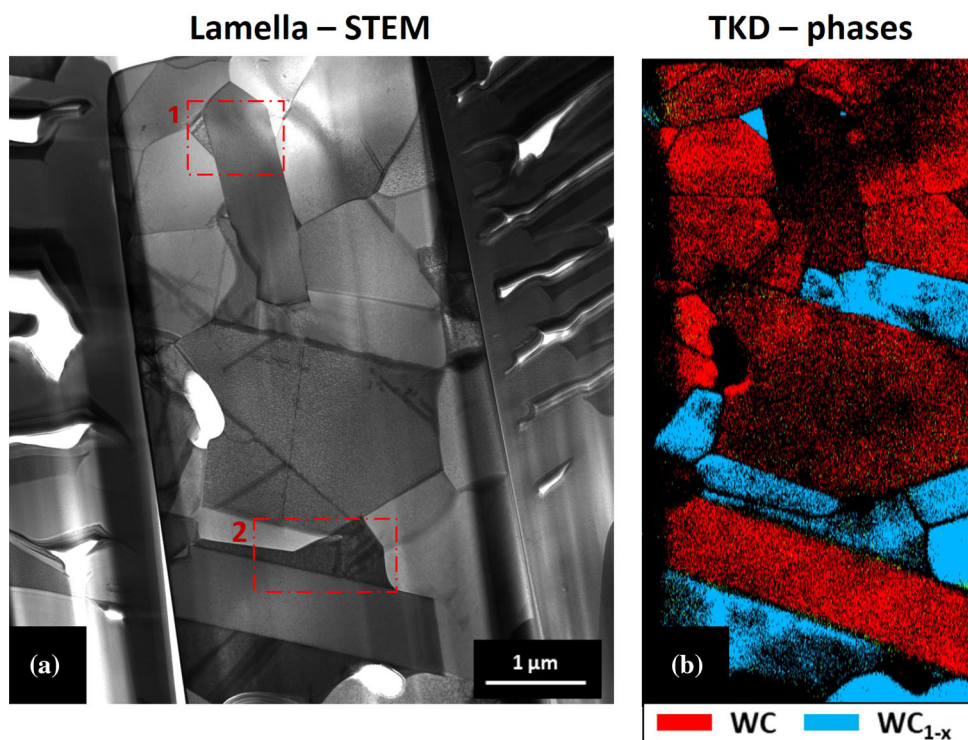
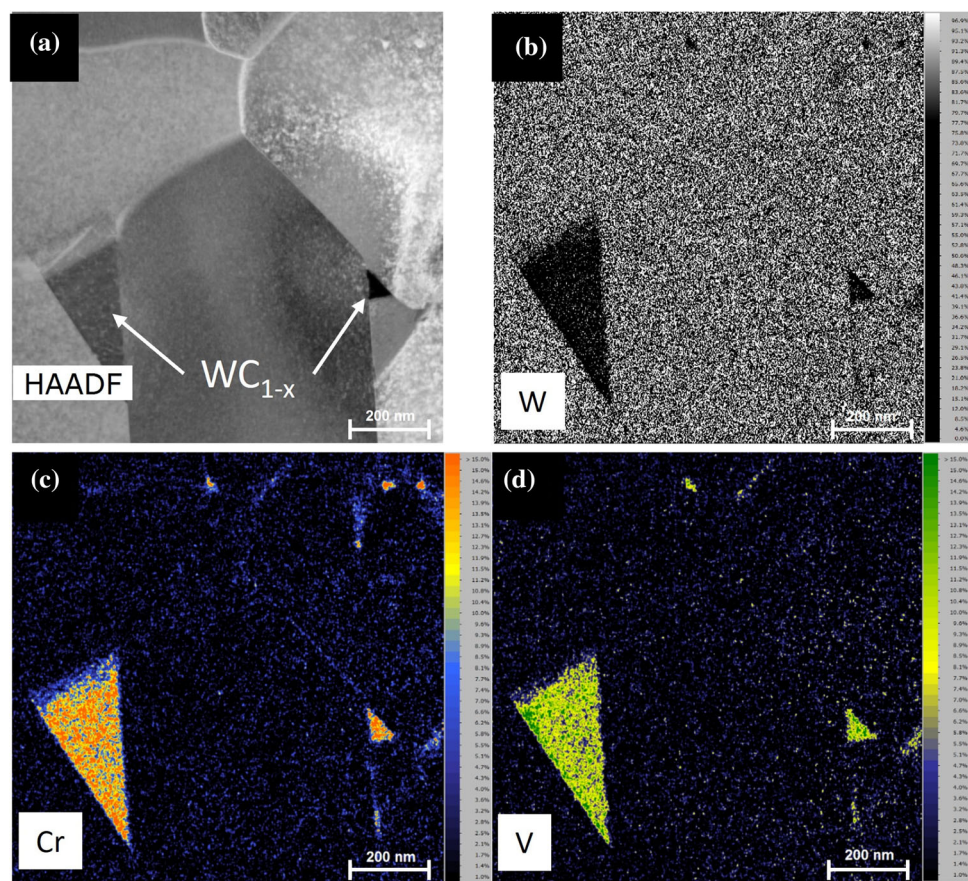


Figure 11 EDXS analysis of the lamella of Fig. 10 (box 1). High-angle annular dark-field (HAADF) micrograph of the analysed area (a); quantitative elemental maps of W (b), Cr (c) and V (d).



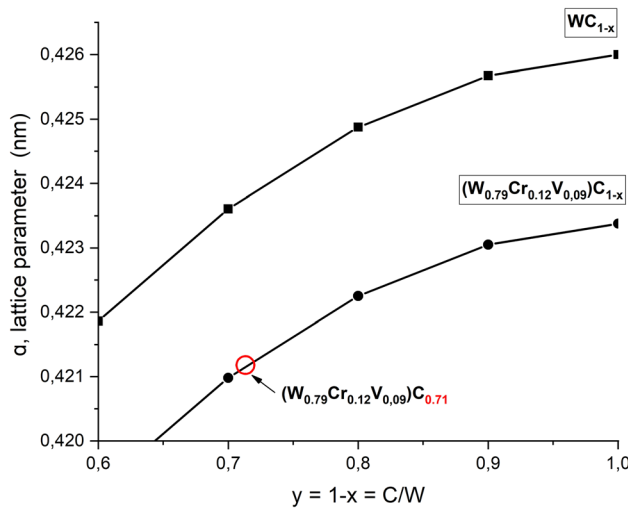


Figure 12 Lattice parameter a as a function of carbon content for cubic tungsten carbides WC_{1-x} (Eq. 1) and the $(\text{W}_{0.79}\text{Cr}_{0.12}\text{V}_{0.09})\text{C}_{1-x}$ modification (Eq. 7). The red circle indicates the resulting carbon content of $(\text{W}_{0.79}\text{Cr}_{0.12}\text{V}_{0.09})\text{C}_{1-x}$ for a lattice parameter of $a = 0.4211 \text{ nm}$, as evaluated from the XRD pattern fitting (Fig. 4).

defect-assisted stabilization mechanism of this high-temperature phase by the flash sintering process.

TEM & transmission Kikuchi diffraction (TKD) analyses

Lamella preparation

An electron transparent portion of the flash sintered material, produced as shown in Fig. 9, can be used to refine with high precision the elemental composition of the cubic phase estimated from XRD analysis to be in between $(\text{W}_{0.8}\text{Cr}_{0.1}\text{V}_{0.1})\text{C}$ and $(\text{W}_{0.6}\text{Cr}_{0.2}\text{V}_{0.2})\text{C}$. The lamella includes several cubic grains, identified as WC_{1-x} in Fig. 10b (ICDD card no. 04-022-5716) by analysing the Kikuchi diffraction patterns in transmission mode (TKD). A portion containing this phase was analysed by EDXS within the TEM, which generated the high-resolution elemental maps of Fig. 11.

As previously stated, the W atoms are partially substituted by Cr and V in the cubic lattice, the elemental map of Fig. 11b clearly showing a lower concentration of tungsten in the grains identified as cubic from the TKD analysis (Fig. 10). All cubic grains (Fig. 10) contain Cr and V as segregated elements, this confirming the EDXS results of Fig. 3 performed on the polished cross section. From the elemental composition, it is possible to determine the

average composition $(\text{W}_{0.79}\text{Cr}_{0.12}\text{V}_{0.09})\text{C}_{1-x}$, very close to that estimated by fitting the occupancy site in the XRD analyses (Fig. 4). The results show that Cr is present in a slightly higher amount than V, in accordance with the higher amount detected in the starting powder (Fig. 1) and in the polished cross section (Fig. 3).

EDXS analysis of the lamella

From the determined composition $(\text{W}_{0.79}\text{Cr}_{0.12}\text{V}_{0.09})\text{C}_{1-x}$ it is possible to estimate the effect of Cr and V on the cubic lattice parameter of WC_{1-x} (Table 1) according to the Vegard's law [28]:

$$a_{A_{(1-x)}B_x} = (1-x)a_A + xa_B \quad (3)$$

where the crystal lattice constant of an alloy $a_{A_{(1-x)}B_x}$ is linearly related to those of its constituent concentrations, $(1-x)$ for A and x for B.

The lattice constant for $(\text{V}_{0.5}\text{W}_{0.5})\text{C}$ and $(\text{Cr}_{0.4}\text{W}_{0.6})\text{C}$ (ICDD cards no. 04-001-6526 and 04-018-1296, respectively) is considered, and the following results are obtained:

$$\begin{aligned} a_{(\text{W}_{0.5}\text{V}_{0.5})\text{C}} &= 0.5a_{\text{WC}} + 0.5a_{\text{VC}} \rightarrow 0.4226 \text{ (nm)} \\ &= 0.5 \cdot 0.426 + 0.5a_{\text{VC}} \rightarrow a_{\text{VC}} = 0.4192 \end{aligned} \quad (4)$$

$$\begin{aligned} a_{(\text{W}_{0.6}\text{Cr}_{0.4})\text{C}} &= 0.6a_{\text{WC}} + 0.4a_{\text{CrC}} \rightarrow 0.4193 \text{ (nm)} \\ &= 0.6 \cdot 0.426 + 0.4a_{\text{CrC}} \rightarrow a_{\text{CrC}} = 0.40925 \end{aligned} \quad (5)$$

The lattice constant of $(\text{W}_{0.79}\text{Cr}_{0.12}\text{V}_{0.09})\text{C}_{1-x}$, in the condition of $\text{C}_{1-x} = \text{C}_1$ ($y = 1$ in Fig. 12), can be calculated from the values of a_{VC} , a_{CrC} and a_{WC} , this latter being the lattice constant of WC_{1-x} evaluated from Eq. 1 at $y = 1$. Therefore:

$$\begin{aligned} a_{(\text{W}_{0.79}\text{Cr}_{0.12}\text{V}_{0.09})\text{C}}(y=1) &= 0.79a_{\text{WC}} + 0.12a_{\text{CrC}} + 0.09a_{\text{VC}} \\ &= 0.4233 \text{ (nm)} \end{aligned} \quad (6)$$

This result can be included in Eq. 1 to consider also the effect of Cr and V on the cubic cell parameter:

$$a_{(\text{W}_{0.79}\text{Cr}_{0.12}\text{V}_{0.09})\text{C}_{1-x}} = 0.4015 - \Delta a + 0.0481y - 0.0236y^2 \quad (7)$$

where $\Delta a = a_{\text{WC}_{1-x}}(y=1) - a_{(\text{W}_{0.79}\text{Cr}_{0.12}\text{V}_{0.09})\text{C}_{1-x}}(y=1) = 0.0026 \text{ [nm]}$

Figure 12 shows the plot of Eqs. 1 and 7. The coupled effect of the substitutional elements (Cr and V) results in a decrease in the WC_{1-x} cubic cell lattice

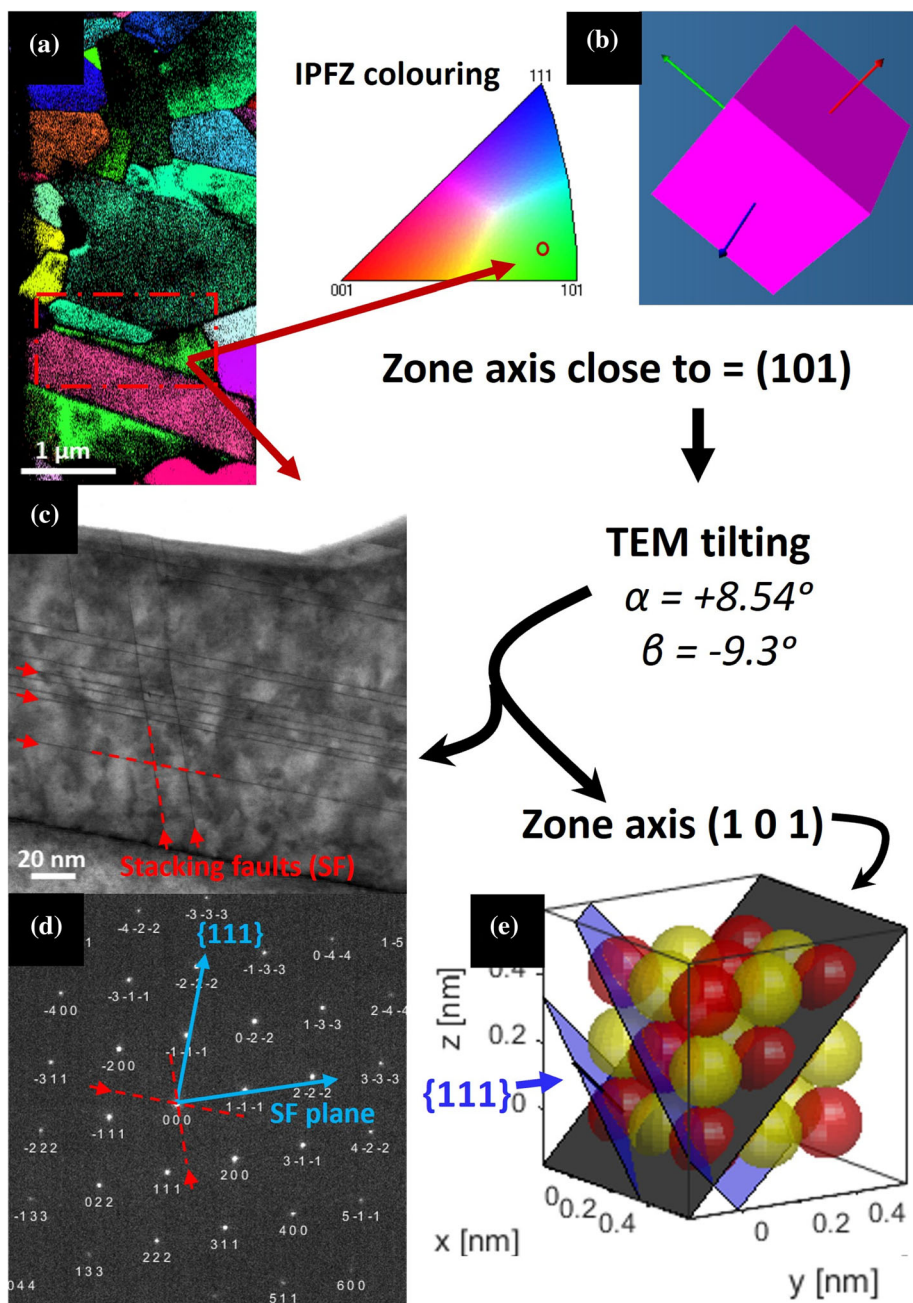
parameter, according to the lower atomic radius of Cr and V with respect to W. The lattice parameter evaluated from the fitting of the experimental diffraction pattern of this new cubic phase (Fig. 4), $a = 0.4211$ nm, can be used in Fig. 12 to estimate the actual carbon content of the $(W_{0.79}Cr_{0.12}V_{0.09})C_{1-x}$ phase which, from Eq. 7, is equal to 0.71. The carbon content of $(W_{0.79}Cr_{0.12}V_{0.09})C_{0.71}$ corresponds to 41–42 at%, a value which now sits correctly within the

carbon stability range of the cubic WC phase of Fig. 5a [1].

Plastic deformation behaviour of cubic tungsten carbide

The portion of the WC grains embodied in the electron transparent lamella of Fig. 10 experienced a high level of stress as shown in Fig. 9d, the original pillar having been subjected to a maximum compressive load of about 8 GPa.

Figure 13 Inverse pole figure zone (IPFZ) map (a) obtained from TKD analysis of the lamella in Fig. 10 (box 2) and (b) orientation of the cubic grain under investigation (red box). STEM micrograph (c) of the cubic WC grain and its selected area electron diffraction pattern (SAED) (d) acquired on the oriented grain, zone axis (101) (e). The orientations of stacking fault planes are represented by red lines (c) translated to blue arrows in the reciprocal lattice (d). Visualization of the zone axis in the cubic WC lattice and its orientation with respect to the stacking faults (SF) planes (e).



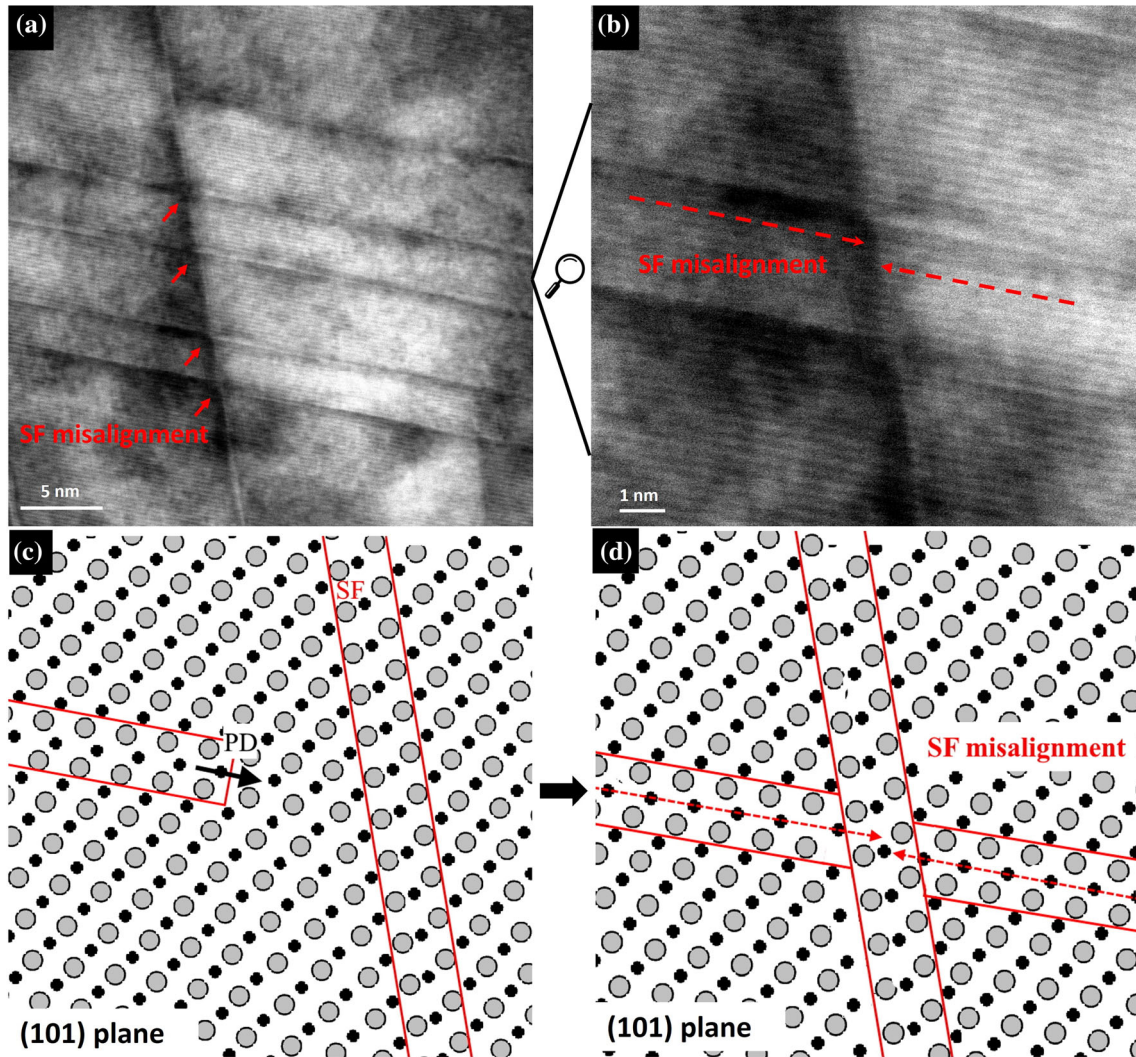
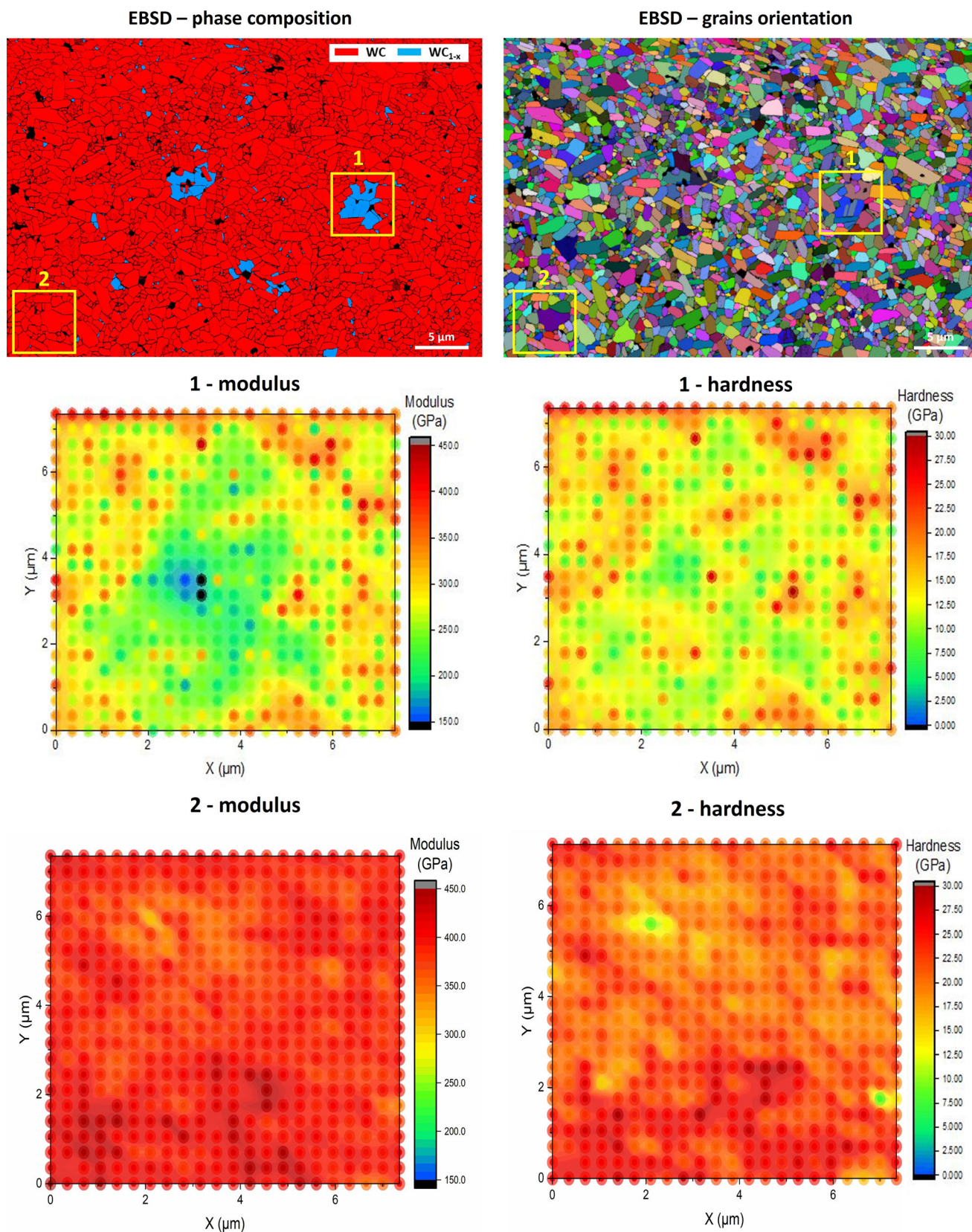


Figure 14 STEM (a) and HR-STEM (b) micrographs of a portion of the cubic WC grain analysed in Fig. 13; the red arrows points the misalignment observed in the SF network. The interaction of moving partial dislocation (PD) with pre-existing SF (c), on the (101) plane, and the generation of SF misalignment (d) is also represented graphically.

During the compression of the WC pillar (Fig. 9), the stress is high enough to overcome the elastic limit of the material, as shown from the stress-strain curve (Fig. 9d). The advantage of this small-scale compression test lies in the possibility of reaching the high stress level required to activate plastic deformation mechanisms in WC before its catastrophic failure [29]. The lamella produced in Fig. 9e contains plastically deformed grains, both hexagonal and cubic, as revealed by the TKD analysis (Fig. 10b). The grains in the lamella exhibit some evidence of dislocation activity as demonstrated by several straight dark bands in hexagonal and cubic grains. It is of

interest for this work the deformative mechanism active in the cubic lattice at room temperature, not reported in the literature. For this reason, the cubic grain in area 2 of Fig. 10a, characterized by high density of such dark bands, was selected for further analyses. This cubic grain (Fig. 13a) is oriented very close to the zone axis (101) as evaluated from the IPFZ map in Fig. 13 (b). The grain appears completely tilted towards the zone axis (101) within TEM. This can be proved by indexing the electron diffraction spot pattern of Fig. 13 (d), acquired on the oriented grain of Fig. 13c, with the CrysTBox software



◀Figure 15 Nanoindentation maps for hardness and reduced elastic modulus acquired on the polished cross section of the flash sintered material; the area analysed by EBSD is a zoom-out view of Fig. 3. Two distinct regions are mapped: in the presence of the cubic phase (area-1) and in an area with hexagonal grains, only (area-2).

algorithm [31] using the cubic crystalline structure-ICDD card no. 04-001-6526, as reference (Fig. 13e).

The oriented grain of Fig. 13c contains a large number of very narrow dark bands, whose nature can be better resolved from the high-resolution images of Fig. 14a & b. The atomic resolution in Fig. 14b allows to discriminate the nature of these defects as stacking faults; the stacking sequence of atomic planes is altered when these dark bands cross the lattice. These SF appears so narrow to be visualized as single lines in Fig. 13c; indeed, in Fig. 14b, the distorted region seems to be limited to single atomic planes. According to the diffraction contrast in TEM analyses, the faulted planes have to be aligned with the direction of the electron beam and, since the grain is oriented with a zone axis (101), all SF planes in Fig. 13c have to be orthogonal with respect to this plane.

The actual SF planes, marked by the red line in Fig. 13c, belong to the {111} system, as proven by the blue line, drawn at 90° with respect to the red lines, in the reciprocal lattice of Fig. 13d. Figure 13e shows a sketch of the cubic cell, where the zone axis (101) (black plane) is perpendicular to the SF planes. These SF are actually the results of plastic deformation driven by the movement and interaction of partial dislocations. It is possible to reach this conclusion from the SF network observed in Fig. 14a & b, when different stacking faults intersect each other's. Following the work of Xiao et al. [30], the SF network is the result of an interaction of partial dislocations with previously formed SF (Fig. 14c); when the shear stress is high enough, the partial can slip away from the intersected SF leaving a misalignment step (Fig. 14d). Thus, the misalignments observed in Fig. 14b can be only caused by the movement and interaction of partial dislocations with previously formed SF creating the complex network shown in Figs. 13c, 14a.

According to these findings, cubic tungsten carbide can be deformed plastically at room temperature through the movement of partial dislocations across {111} planes. For comparison, the system

{111} < 110 > is a well-known primary slip system in FCC metals, although in nonstoichiometric cubic transition-metal carbides, such as TiC, VC, and ZrC, different slip systems result active at room temperature, like {110} < 110 > or, more rarely, {001} < 110 > [31]. Several researcher argued that the characteristic brittle-to-ductile transition of these cubic transition-metal carbides is attributed to the activation of the slip system {111} < 110 > at high temperature, by a partial weakening of the strong directional M-C bonds that limit slip on such a plane [31–34]. In this perspective, cubic WC may possess a higher room temperature plasticity in comparison with other cubic carbides with similar rock-salt structure.

Nanoscale mechanical properties: hardness & elastic modulus maps

Cubic WC is characterized by a noticeable lower hardness and elastic modulus with respect to the hexagonal phase. The nanoindentation analysis of Fig. 15 (1) shows how the elastic modulus (E) of the cubic phase is about 230–310 GPa, considerably lower than that of WC (650–700 GPa). The hardness follows the same behaviour, with a drop from 30 down to 10–15 GPa. Shanenkov et al. obtained similar results (Young's modulus \approx 300 GPa, hardness \approx 10–25 GPa) from nanoindentation in pure WC_{1-x} thin film, deposited on a metallic surface by high-speed plasma spraying [35]. The comparison between phase composition and grain orientation discloses the effect of this latter on small-scale properties; elastic modulus and hardness of area-2 show small variations in proximity of small pores, but not between differently oriented grains. In this perspective, the noticeable difference in E and H in the region around the cubic grains (Fig. 15 1) can be only addressed to the presence of cubic grains, which somehow affects the elastic modulus and hardness of the adjacent material.

The atomic force microscope (AFM) maps (Fig. 16) shows the condition of the surface reached after the polishing procedure. Directional scratches caused during polishing and small residual pores are present in both area-1 and area-2. In particular, the area containing the cubic phase, $(W_{0.79}Cr_{0.12}V_{0.09})C_{0.71}$, results in a strong contrast in both imaging modes, gradient (μ N) and topographic (nm). The dark topographic contrast of area-1 identified as cubic by EBSD

Figure 16 Atomic force microscopy (AFM) images taken in area-1 and area-2 of Fig. 15 prior to nanoindentation testing.

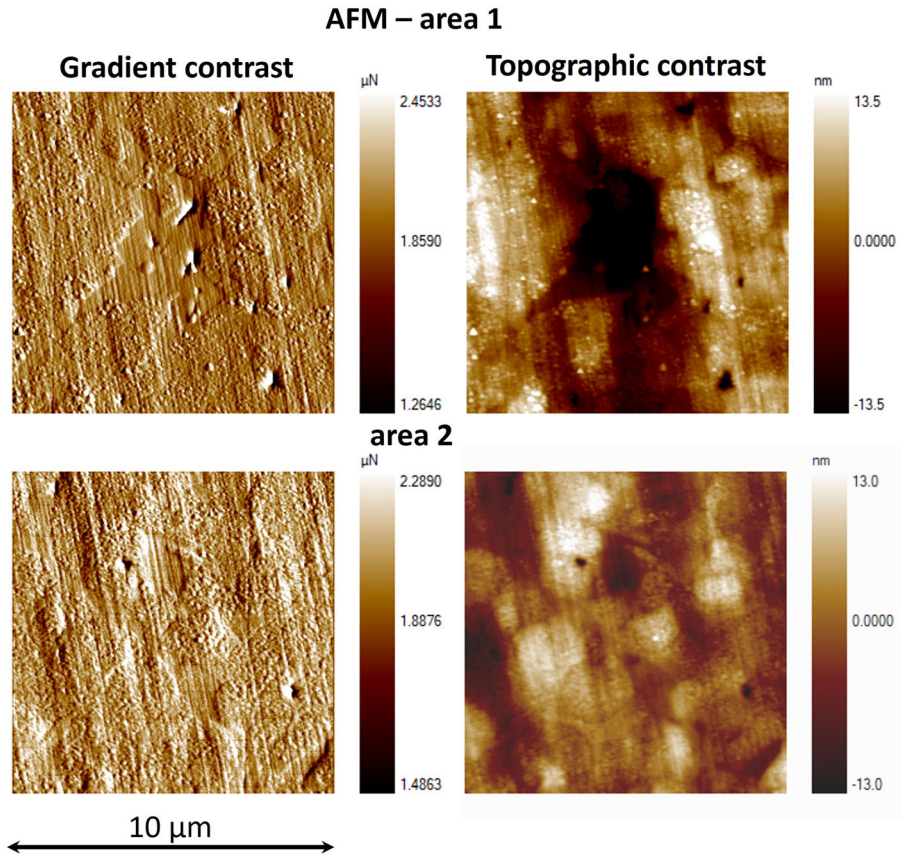


(Fig. 15, (1)) corresponds to a small depression on the surface, which is absent in the area without the cubic phase (Fig. 16 2). This can be the result of a larger material removing rate from the surface upon polishing; the cubic phase, being softer than WC, is removed more quickly leaving a small depression on the surface as shown by the AFM images of area-1.

Conclusions

Cubic tungsten carbide was successfully obtained as a second phase during the electrical resistance flash sintering (ERFS) of commercial WC nanopowders. The low oxygen content in the nanopowders limits the decarburization phenomenon, thus avoiding the $\text{WC} \rightarrow \text{W}_2\text{C}$ transformation during both SPS and ERFS processes. However, only during the flash process, the limited loss of structural carbon and the unconventional high sintering rate allow to produce and stabilize the high-temperature WC_{1-x} structure rather than W_2C .

Cubic tungsten carbide was characterized as $(\text{W}_{0.87}\text{Cr}_{0.12}\text{V}_{0.09})\text{C}_{0.71}$ with a lattice constant of

$a = 4.211 \text{ \AA}$, which disagrees with the ICDD card no. 04-022-5716 ($a = 4.234 \text{ \AA}$) due to the presence of Cr and V in solid solution. Phase stability simulation (CALPHAD) of the W–C–Cr–V quaternary systems reveals an opposite role of Cr and V on WC_{1-x} phase stability and their simultaneous presence in $(\text{W}_{0.87}\text{Cr}_{0.12}\text{V}_{0.09})\text{C}_{0.71}$ does not explain its stability. Vacuum annealing experiments determine the decomposition of $(\text{W}_{0.87}\text{Cr}_{0.12}\text{V}_{0.09})\text{C}_{0.71}$ into WC and W_2C products in the 700–1100°C temperature range, thus pointing out its metastable character.

The $(\text{W}_{0.87}\text{Cr}_{0.12}\text{V}_{0.09})\text{C}_{0.71}$ cubic phase is softer than WC, with an hardness ranging from 10 to 15 GPa and an elastic modulus of about 230–310 GPa. Cubic grains reveal a high amount of stacking faults arranged in a network of narrow bands perpendicular to each other's, this network being the result of partial dislocations interacting with {111} stacking fault planes.

The results reported in this work point out the great advantage of the ERFS process to produce new composite materials based on WC/ WC_{1-x} . The softer character and the room temperature plasticity, via

{111} active slip planes, make cubic WC a potential candidate to optimize the hardness/toughness ratio of tungsten carbides products.

Acknowledgements

This work was partially supported within the program Departments of Excellence 2018–2022 (DII-UNITN “E-Mat”) – funded by the Italian Ministry of University and Research (MIUR)

Authors' contribution

IM: Conceptualization, Methodology, Software, Validation, Formal analysis, Investigation, Data Curation, Writing—Original Draft, and Visualization. JMMA: Resources, Supervision, and Project administration. AM: Resources, Funding acquisition. VMS: Project definition, planning, management and administration, Writing—Review & Editing, Supervision, Resources, and Funding acquisition.

Data and code availability

The raw and processed data used to produce this work will be shared by the corresponding author upon reasonable request.

Declarations

Conflict of interest The authors have no conflicts of interest or competing interests to declare that are relevant to the content of this article.

References

- [1] Kurlov AS, Gusev AI (2006) Tungsten carbides and W–C phase diagram. *Inorg Mater* 42:121–127. <https://doi.org/10.1134/S0020168506020051>
- [2] Zhang FG, Zhu XP, Lei MK (2012) Microstructural evolution and its correlation with hardening of WC–Ni cemented carbides irradiated by high-intensity pulsed ion beam. *Surf Coatings Technol* 206:4146–4155. <https://doi.org/10.1016/j.surfcoat.2012.04.011>
- [3] Pak A, Sivkov A, Shanenkov I, Rahmatullin I, Shatrova K (2015) Synthesis of ultrafine cubic tungsten carbide in a discharge plasma jet. *Int J Refract Met Hard Mater* 48:51–55. <https://doi.org/10.1016/j.ijrmhm.2014.07.025>
- [4] Tanaka S, Bataev I, Oda H, Hokamoto K (2018) Synthesis of metastable cubic tungsten carbides by electrical explosion of tungsten wire in liquid paraffin. *Adv Powder Technol* 29:2447–2455. <https://doi.org/10.1016/j.apt.2018.06.025>
- [5] Zhang FG (2019) Friction and wear behavior of WC/Ni cemented carbide tool material irradiated by high-intensity pulsed electron beam. *Ceram Int* 45:15327–15333. <https://doi.org/10.1016/j.ceramint.2019.05.025>
- [6] Lian Y, Han B, Liu D, Wang Y, Zhao H, Xu P, Han X, Du Y (2020) Solvent-free synthesis of ultrafine tungsten carbide nanoparticles-decorated carbon nanosheets for microwave absorption. *Nano-Micro Lett* 12:1–13. <https://doi.org/10.1007/s40820-020-00491-5>
- [7] Abad MD, Muñoz-Márquez MA, El Mrabet S, Justo A, Sánchez-López JC (2010) Tailored synthesis of nanostructured WC/a-C coatings by dual magnetron sputtering. *Surf Coatings Technol* 204:3490–3500. <https://doi.org/10.1016/j.surfcoat.2010.04.019>
- [8] Biesuz M, Sglavo VM (2020) Beyond flash sintering: how the flash event could change ceramics and glass processing. *Scr Mater* 187:49–56. <https://doi.org/10.1016/j.scriptamat.2020.05.065>
- [9] Biesuz M, Grasso S, Sglavo VM (2020) What's new in ceramics sintering? A short report on the latest trends and future prospects. *Curr Opin Solid State Mater Sci* 24:100868. <https://doi.org/10.1016/j.cozsms.2020.100868>
- [10] Mazo I, Molinari A, Sglavo VM (2022) Electrical resistance flash sintering of tungsten carbide. *Mater Des* 213:110330. <https://doi.org/10.1016/j.matdes.2021.110330>
- [11] Inframat advanced materials, tungsten carbide nano powder, (1996). <http://www.advancedmaterials.us/74N-0601.htm> Accessed Dec 13 2021.
- [12] Mazo I, Molinari A, Sglavo VM (2022) Effect of pressure on the electrical resistance flash sintering of tungsten carbide. *J Eur Ceram Soc* 42:2028–2038. <https://doi.org/10.1016/j.jeurceramsoc.2022.01.017>
- [13] Mazo I, Vanzetti LE, Molina-Aldareguia JM, Molinari A, Sglavo VM (2022) Role of surface carbon nanolayer on the activation of flash sintering in tungsten carbide. *Int J Refract Met Hard Mater* 106090. <https://doi.org/10.1016/j.ijrmhm.2022.106090>
- [14] Suzuki S (2013) Features of transmission EBSD and its application. *Jom* 65:1254–1263. <https://doi.org/10.1007/s11837-013-0700-6>
- [15] Sun J, Zhao J, Huang Z, Yan K, Shen X, Xing J, Gao Y, Jian Y, Yang H, Li B (2020) A rev bind tungsten carbide: dev appl. *Nano Micro Lett*. <https://doi.org/10.1007/s40820-019-0346-1>
- [16] Shanenkov I, Nikitin D, Ivashutenko A, Shanenkova Y, Vympina Y, Butenko D, Han W, Sivkov A (2021) Studies on

- the thermal stability of nanosized powder of WC_{1-x}-based product prepared by plasma dynamic method, compaction feasibility of the powder and preparation of composite with aluminium. *Ceram Int* 47:6884–6895. <https://doi.org/10.1016/j.ceramint.2020.11.035>
- [17] Al-Aqeeli N (2015) Characterization of nano-cemented carbides Co-doped with vanadium and chromium carbides. *Powder Technol* 273:47–53. <https://doi.org/10.1016/j.powtec.2014.12.032>
- [18] Sugiyama I, Mizumukai Y, Taniuchi T, Okada K, Shirase F, Tanase T, Ikuhara Y, Yamamoto T (2012) Formation of (W, V)Cx layers at the WC/Co interfaces in the VC-doped WC-Co cemented carbide. *Int J Refract Met Hard Mater* 30:185–187. <https://doi.org/10.1016/j.ijrmhm.2011.08.006>
- [19] Yousfia MA, Norgren S, Andrén HO, Falk LKL (2018) Chromium segregation at phase boundaries in Cr-doped WC-Co cemented carbides. *Mater Charact* 144:48–56. <https://doi.org/10.1016/j.matchar.2018.06.034>
- [20] Lay S, Hamar-Thibault S, Lackner A (2002) Location of VC in VC, Cr₃C₂ codoped WC-Co cermets by HREM and EELS. *Int J Refract Met Hard Mater* 20:61–69. [https://doi.org/10.1016/S0263-4368\(01\)00071-3](https://doi.org/10.1016/S0263-4368(01)00071-3)
- [21] Gao Y, Song X, Liu X, Wei C, Wang H, Guo G (2013) On the formation of WC 1-x in nanocrystalline cemented carbides. *Sci Mater* 68:108–110. <https://doi.org/10.1016/j.scriptamat.2012.09.016>
- [22] Cho J, Li Q, Wang H, Fan Z, Li J, Xue S, Vikrant KSN, Wang H, Holland TB, Mukherjee AK, García RE, Zhang X (2018) High temperature deformability of ductile flash-sintered ceramics via in-situ compression. *Nat Commun* 9:1–9. <https://doi.org/10.1038/s41467-018-04333-2>
- [23] Phuah XL, Cho J, Tsakalakos T, Mukherjee AK, Wang H, Zhang X (2021) Defects in flash-sintered ceramics and their effects on mechanical properties. *MRS Bull* 46:44–51. <https://doi.org/10.1557/s43577-020-00014-y>
- [24] Li J, Cho J, Ding J, Charalambous H, Xue S, Wang H, Phuah XL, Jian J, Wang X, Ophus C, Tsakalakos T, Edwin García R, Mukherjee AK, Bernstein N, Stephen Hellberg C, Wang H, Zhang X (2019) Nanoscale stacking fault-assisted room temperature plasticity in flash-sintered TiO₂. *Sci Adv* 5:1–10. <https://doi.org/10.1126/sciadv.aaw5519>
- [25] Li W, Chen L, Liu D, Liu J, An L (2021) Ultra-low temperature reactive flash sintering synthesis of high-enthalpy and high-entropy Ca_{0.2}Co_{0.2}Ni_{0.2}Cu_{0.2}Zn_{0.2}O oxide ceramics. *Mater Lett* 304:130679. <https://doi.org/10.1016/j.matlet.2021.130679>
- [26] Rempel A, Würschum R (2000) Atomic defects in hexagonal tungsten carbide studied by positron annihilation. *Phys Rev B-Condens Matter Mater Phys* 61:5945–5948. <https://doi.org/10.1103/PhysRevB.61.5945>
- [27] Burr PA, Oliver SX (2019) Formation and migration of point defects in tungsten carbide: Unveiling the sluggish bulk self-diffusivity of WC. *J Eur Ceram Soc* 39:165–172. <https://doi.org/10.1016/j.jeurceramsoc.2018.10.001>
- [28] Denton AR, Ashcroft NW (1991) Vegards law. *Phys Rev A* 43:3161–3164. <https://doi.org/10.1103/PhysRevA.43.3161>
- [29] Dehm G, Jaya BN, Raghavan R, Kirchlechner C (2018) Overview on micro-and nanomechanical testing: new insights in interface plasticity and fracture at small length scales. *Acta Mater* 142:248–282. <https://doi.org/10.1016/j.actamat.2017.06.019>
- [30] Xiao J, Wu N, Ojo O, Deng C (2021) Stacking fault and transformation-induced plasticity in nanocrystalline high-entropy alloys. *J Mater Res* 36:2705–2714. <https://doi.org/10.1557/s43578-021-00140-6>
- [31] Kiani S, Yang JM, Kodambaka S (2015) Nanomechanics of refractory transition-metal carbides: a path to discovering plasticity in hard ceramics. *J Am Ceram Soc* 98:2313–2323. <https://doi.org/10.1111/jace.13686>
- [32] Kohlstedt DL (1973) The temperature dependence of microhardness of the transition-metal carbides. *J Mater Sci* 8:777–786. <https://doi.org/10.1007/BF02397907>
- [33] Hannink RH, Kohlstedt DL, Murray MJ (1972) Slip system determination in cubic carbides by hardness anisotropy. *Proc R Soc London A Math Phys Sci* 326:409–420. <https://doi.org/10.1098/rspa.1972.0017>
- [34] Yu H, Bahadori M, Thompson GB, Weinberger CR (2017) Understanding dislocation slip in stoichiometric rocksalt transition metal carbides and nitrides. *J Mater Sci* 52:6235–6248. <https://doi.org/10.1007/s10853-017-0857-4>
- [35] Shanenkov I, Nikitin D, Ivashutenko A, Rahmatullin I, Shanenkova Y, Nassyrbayev A, Han W, Sivkov A (2020) Hardening the surface of metals with WC_{1-x} coatings deposited by high-speed plasma spraying. *Surf Coatings Technol* 389:125639. <https://doi.org/10.1016/j.surco.2020.125639>

Publisher's Note Springer Nature remains neutral with regard to jurisdictional claims in published maps and institutional affiliations.

Springer Nature or its licensor (e.g. a society or other partner) holds exclusive rights to this article under a publishing agreement with the author(s) or other rightsholder(s); author self-archiving of the accepted manuscript version of this article is solely governed by the terms of such publishing agreement and applicable law.